Composite Structures 366 (2025) 119198

Contents lists available at ScienceDirect

Composite Structures

journal homepage: www.elsevier.com/locate/compstruct

Development of an effective modelling method for the mechanical analysis of submarine power cables under bending

Pan Fang [a],*, Xiao Li [b],*, Xiaoli Jiang [a], Hans Hopman [a], Yong Bai [c]

[a] Department of Maritime and Transport Technology, Delft University of Technology, Netherlands
[b] Institute of High Performance Computing (IHPC), Agency for Science, Technology and Research (A*STAR), 1 Fusionopolis Way, #16-16 Connexis, Singapore 138632, Republic of Singapore
[c] College of Civil Engineering and Architecture, Zhejiang University, Hangzhou, Zhejiang, PR China

ARTICLE INFO

Keywords:
Periodical boundary conditions
Damping
Initial residual stress
Bending
Submarine power cables

ABSTRACT

The complex interplay of numerous helical components within submarine power cables (SPCs), especially those with significant contact issues due to initial residual stress, complicates their modelling and limits our understanding of these structures. In this paper we proposed an effective modelling method designed for the local mechanical analysis of SPCs under bending. The method was developed based on three key aspects: (1) constructing appropriate finite elements to reduce the number of elements required; (2) employing contact damping to address the effects of initial residual stress at contact interfaces; and (3) applying periodic boundary conditions on a repeated unit cell (RUC) to reduce the model size. The accuracy of this method was validated through extensive testing on both single-core and three-core SPC samples, and its efficiency was confirmed by comparing these results with those obtained from traditional full-scale models. Following validation, the model was employed to illustrate the local mechanical behaviours of SPCs under bending, both at the overall level and at the component level. This model serves as a powerful tool for cable engineers, offering deeper insights into the internal interplays of SPCs. All relevant codes developed in this paper are freely available at https://pan-fang.github.io/Codes/.

1. Introduction

Submarine power cables (SPCs) are essential for transmitting electricity in the offshore wind industry. As wind farms expand into more remote and deeper ocean regions to tap into richer wind resources, the operational environment for SPCs becomes increasingly harsh. This is especially true for cables suspended from floating platforms, as illustrated in Fig. 1. These cables, known as dynamic power cables, are subjected to dynamic loadings from currents, waves, and platform movements. Such conditions have resulted in failures, including fatigue, which pose significant challenges to the durability of these cables [1–3].

Addressing the failures of SPCs requires a comprehensive understanding of their local mechanical behaviours [1,4,5]. However, the complex structural configuration and contact issues pose significant challenges, particularly in multi-core SPCs. This is evident in the single-core and three-core configurations depicted in Fig. 2, with the materials and functions of the main components detailed in Table 1. Unlike single-core SPCs, the inner components of three-core SPCs, such as the conductors, are also designed in helical shapes, in addition to the helical wires in the armour layers. These helical components are intended to mitigate built-up stress during loading by allowing slippage between components, thereby extending the cable's lifespan. However, they also make the local mechanical analysis of three-core SPCs even more complex.

Before moving to the study of the overall structure, researchers put much effort in the investigation of the single components in power cables. Fouad and Monssef [6], for example, studied the plasticity evolution and predict the damage of conductors by modelling all the helical wires and considering the contact issues within their interfaces. Nasution et al. and Jiang et al. [7–9] also examined the fatigue behaviour of helical conductors with more complex configurations, validating their numerical models with test data. In recent years, more investigations [10–12] into insulation layers have appeared in the public literature, aiming to understand how electrical and thermal fields affect the insulation layer. However, to study the overall behaviour of SPCs, some simplifications have to be made considering current computational capacity. Common simplifications in studying the overall SPC include modelling the inner copper conductors as solid components and

* Corresponding authors.
E-mail addresses: panfang@zju.edu.cn (P. Fang), li_xiao@ihpc.a-star.edu.sg (X. Li).

https://doi.org/10.1016/j.compstruct.2025.119198
Received 16 November 2024; Received in revised form 1 April 2025; Accepted 10 April 2025
Available online 24 April 2025

Symbols and Abbreviations

p	Pitch length
m	Number of helix
T	Tension
θ	Bending angle
$\boldsymbol{U}, u$	Displacement vector and its components
$\boldsymbol{X}, X$	Coordinate vector and its components
$\boldsymbol{\phi}, \phi$	Rotation vector and its components
$\boldsymbol{R}$	Rotation matrix
$\boldsymbol{F}$	Force vector
$\boldsymbol{M}$	Moment vector
SPC	Submarine power cable
RP	Reference point
RUC	Repetitive unit cell
FE	Finite element
FEM	Finite element method
DOF	Degree of freedom
$B.C.$	Boundary condition
PE	Polyethylene

ignoring the effects of thermal or electrical fields [13–17]. The present study focuses specifically on the mechanical behaviour of the overall power cable. As such, similar simplifications are applied in line with established practice in the field.

For such a complex structure with strong nonlinearity, a 3D finite element model based on numerical methods is more suitable for gaining deeper insights into the local mechanical behaviours than analytical methods [13,18]. However, modelling a structure with numerous components, particularly the helical components, demands substantial computational resources. Additionally, the intensive contact between components can lead to significant convergence issues. To develop an effective (accurate and efficient) modelling method for SPCs, it is crucial to reduce the number of finite elements and address the contact challenges appropriately.

The number of finite elements can be reduced using two approaches. The first approach involves constructing components with an element type that requires fewer finite elements. In the work by Fang et al. [18], for example, all helical wires are simulated using beam elements instead of solid elements, which reduces the number of elements and consequently enhances computational efficiency. This simplification is acceptable in tension cases where the stick–slip issue is not significant. Sævik [19] introduced an eight-degree-of-freedom curved beam element, based on Kirchhoff rod theory [20,21], that restricts transverse translation. This element allows the wire to follow a loxodromic slip path, improving the model's fidelity to actual helical behaviour. The numerical program incorporating similar elements has been well-developed and commercialized, as demonstrated in studies by Skeie et al. [22] and DNV [23], highlighting their practical applicability in the industry. Meshing wires using solid elements can lead to excessive density, which is computationally expensive. Based on advancements in modelling helical ropes [24], Menard and Cartraud [25] employed a hybrid approach using both beam and surface elements to effectively simulate the helical wires in ropes. The beams are meshed using Timoshenko beam elements, and the surface elements, which lack thickness or stiffness, are coupled at the nodes with the beams. This method has demonstrated a strong ability to balance computational efficiency and accuracy [24,25].

The second approach to reducing the number of finite elements is by shortening the model size, specifically in the axial direction. However, length of the model cannot be shortened arbitrarily, as it is known that the boundary effects due to short length can influence the mechanical behaviours of structures with helical components [18,29,30]. Currently, there is no definitive guidance on determining the full model

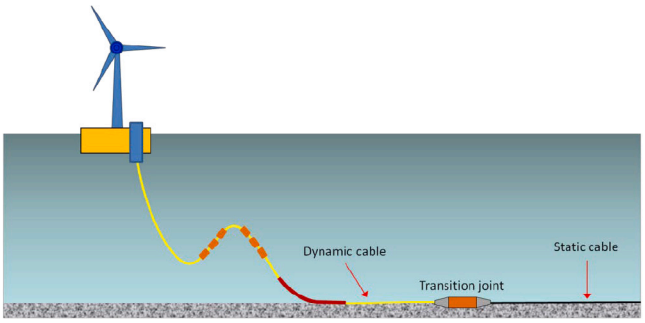

Fig. 1. Facilities in floating wind system [26].

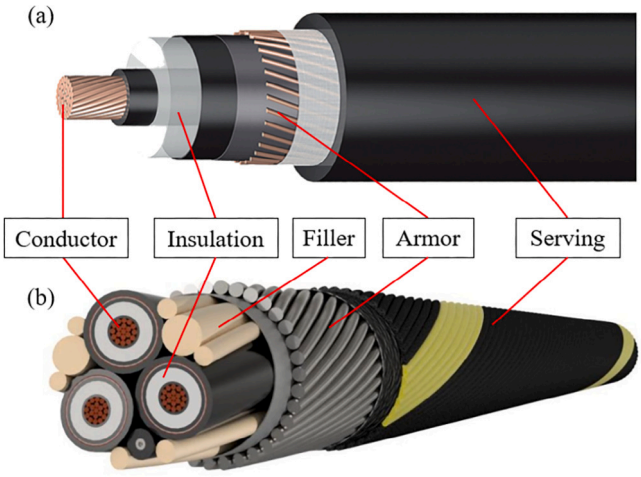

Fig. 2. Typical configuration of a one-core SPC (a) [27] and a three-core SPC (b) [28].

Table 1
Main components inside a cable.

Component	Material	Function
Conductor	Copper/Aluminium	Electricity transportation
Insulation	Cross-linked polyethene	Prevent electrical leakage
Armour	Steel	Provide mechanical protection
Serving	Polymer	Anti-corrosion

length necessary to accurately capture the mechanical behaviours of SPCs under bending. Theoretically, the longer the model, the more effectively the boundary effects are eliminated, leading to more accurate results [29]. However, a model that is too long, containing a substantial number of elements, can make the calculation impractical for such a complex structure. Due to the repetitive structural configuration of the helical components within SPCs, using a repetitive unit cell (RUC) model with periodic boundary conditions is a promising approach to shorten the length of the model [13,15–17]. However, no researchers have yet developed appropriate theoretical framework for both single-core and multi-core SPCs.

Regarding the contact issue, the challenges arise not only in the tangential direction but also in the normal direction. The tangential contact involves constructing an appropriate frictional model. The Coulomb friction model is classical and has been extensively used to describe tangential contact properties [17,31–33]. This model characterizes the frictional behaviour between surfaces using a coefficient of friction [34]. Researchers have also explored other friction models. For instance, Dai et al. [35] examined the mechanical behaviour of a flexible pipe using four different friction models, revealing that the pipe exhibits different behaviours under each condition. It is important to note that friction properties can vary even within the same flexible

structure, as the contact interfaces are not identical. For example, the friction coefficients between two polymer interfaces differ from those between polymer and metal. Additionally, the friction coefficient can be influenced by various factors such as temperature [36] and air moisture content [37]. Measuring friction coefficients is also a complex task. As a result, an equivalent unified friction coefficient is typically adopted for the structure [38–40].

The challenge in analysing normal contact lies in determining the normal stress within SPCs, which is largely induced by initial residual stresses generated during the manufacturing process, particularly from the extrusion of polymer materials [41]. These stresses are increasingly recognized as significant factors in the stick–slip behaviour of multi-layer flexible structures [42–44]. Kraincanic and Kebadze [43] emphasized the importance of initial interlayer pressures, which should be included with pipe construction data for accurate analysis, though these values are difficult to measure directly through testing [41]. Fernando suggested methods such as neutron diffraction to measure these values in the pressure/tensile armour wires of flexible pipes [45]. However, since initial residual stresses vary within an SPC, it is recommended to use the curvature–bending moment curve from bending tests to calibrate an equivalent external pressure that simulates the effects of initial residual stress [15,41]. In studies of other flexible structures, strategies to address initial residual stress include applying internal pressure, a tensile force, or introducing a thermal field to induce radial stresses within the structure [46–48]. However, these methods require an additional analysis step, which significantly increases computational demands.

The challenges in developing such a modelling method primarily converge into three key areas: the establishment of finite elements, the setup of contact models, and the formulation of boundary conditions. This paper aims to enable the local mechanical analysis of both single-core and multi-core SPCs under bending. To this end, a modelling method for the local mechanical analysis of SPCs under bending is proposed. The structure of the paper is as follows: Section 2 outlines the methodology. Section 3 describes the necessary tests conducted for validation purposes. The model under bending, based on the proposed method, is validated in Section 4. Following validation, the efficiency and accuracy of the RUC model are compared against traditionally-built full-scale models in Section 5. The local mechanical analysis of SPCs under bending is detailed in Section 6. Finally, Section 7 presents the conclusions.

2. Methodology

The three challenges in developing such a modelling method will be solved one by one in this section. An effective model based on the modelling method for the local mechanical analysis of SPCs will be given at the end.

This section is structured aligning with the three challenges as follows: the element type will be introduced in Section 2.1. The contact issue will be solved in Section 2.2. Afterwards, the boundary conditions for SPCs are presented in Section 2.3. Note that the methodology presented here is universal and not confined to any specific finite element (FE) code. Readers can construct an appropriate numerical model according to their preferences based on the principles of this methodology.

2.1. The establishment of finite elements

The cross-section of an SPC is inherently complex, featuring numerous components that require discretization into a large number of elements for finite element modelling. To enhance computational efficiency, we adopt a technique inspired by Bussolati's work on helical ropes [24], utilizing a combination of beam and surface elements to simulate the helical wires and metals within SPCs. This approach significantly reduces the number of elements in the model, as demonstrated in Fig. 3. Due to prevalent contact issues in the analysis, surface elements are employed to enable beam elements to capture contacts effectively by coupling the nodes on the surface with their corresponding master nodes on a beam. For the beams and surfaces, Timoshenko beam elements and non-structural surface elements are used, respectively. Timoshenko beam theory, which accounts for shear deformation and rotary inertia, provides a more accurate prediction of deformation and stress compared to the simpler Euler–Bernoulli beam theory. The surface elements, crucial for modelling contacts, are designed to be non-structural, possessing neither thickness nor inherent stiffness.

The reference node on the beam has displacement $\boldsymbol{U}$ and rotation $\boldsymbol{\phi}$ degrees of freedom (DOF), while the nodes on the surface have three DOFs $\boldsymbol{U}$. The relations between the RP and the corresponding nodes on the same cross-section can be described below:

$$\begin{cases} \sum_n \boldsymbol{F}^i = \boldsymbol{F}^{RP} \\ \sum_n \boldsymbol{X}^i \times \boldsymbol{F}^i = \boldsymbol{M}^{RP} + \boldsymbol{X}^{RP} \times \boldsymbol{F}^{RP} \end{cases} \tag{1}$$

where $\boldsymbol{F}$ and $\boldsymbol{M}$ are the load and moment, while $\boldsymbol{X}$ is the position of the corresponding point. i is the node sequence on the coupled cross-section, and n is the total number of nodes. The coupling approach has been proved to provide a very good compromise between accuracy and computational efficiency [24,25]. This will also be verified in Section 4 before it is applied for further analysis.

2.2. The setup of contact

As mentioned in the Introduction, the necessary factors related to contact behaviours are normal contact property, tangential contact property and the initial residual stress, in which the friction coefficient in the tangential direction and the equivalent external pressure in simulating the residual stress are most important and should be provided. Both values are the intrinsic properties of a sample, and in the industry of flexible pipes, they are supposed to be provided alongside the pipe construction data [43]. CIGRE [41] has pointed out a way to obtain the equivalent external pressure, i.e., calibrating it by the curvature–bending moment curve. In fact, Menard and Cartraud [15] calibrated both the friction coefficient and the equivalent external pressure by the curvature–bending moment curves from their bending test, considering the fact that the friction coefficients are also difficult to test directly in practice.

To minimize the parameters that need to be calibrated through testing, a new method for addressing the contact issue is proposed, namely the introduction of contact damping into the cable system. Contact damping can reduce the relative motion among interfaces and slow down slippage. In the finite element method (FEM), damping can be added to a structure by incorporating damper elements such as dashpots, connectors, or springs [34]. However, these methods require additional elements within the structure, which increases the computational resources needed. Therefore, in the proposed model, a constant contact damping coefficient is applied to the interfaces of SPCs. The damping forces can be calculated with:

$$f_{vd} = \mu A v_{rel} \tag{2}$$

where A represents the nodal area, and v_{rel} is the rate of relative motion between the two surfaces. The damping coefficient μ should be provided as a constant with units of pressure divided by velocity. For example, in the International System of Units, it would be expressed as $\frac{\mathrm{N}}{\mathrm{m}^2} / \frac{\mathrm{m}}{\mathrm{s}}$. The proposed model is intended to handle a quasi-static system subjected to loads or changes that occur slowly enough for the rate of relative motion to remain stable throughout the process. Consequently, the damping force in the tangential direction is also nearly stable. This stability can be verified by monitoring the damping energy during the simulation process.

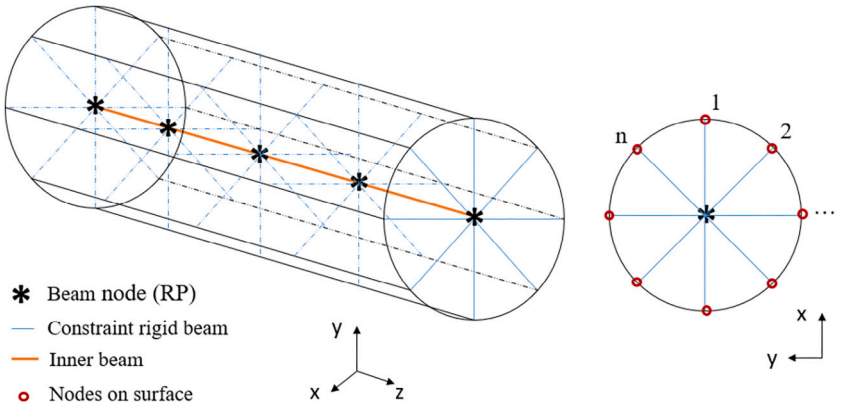

Fig. 3. The combination of beam and surface elements.

This method offers several advantages. First, it simplifies the process by equating the friction coefficient and initial residual stress through a single parameter: the damping coefficient. Second, unlike the method of applying equivalent external pressure, adding contact damping does not require an additional analysis step, thereby accelerating the overall calculation process and conserving computational resources. Third, the damping coefficient is easily adjustable within the SPC for specific contact interfaces, which is particularly convenient during the design process where sensitivity studies are often conducted. Finally, the introduction of damping also enhances the model's convergence.

2.3. The formulation of boundary conditions

Given the special structural configuration of components in an SPC, periodic boundary conditions (B.C.) can be imposed on both ends to minimize boundary effects and expedite calculations by reducing model length. SPCs can utilize periodic B.C. derived from the homogenization method applicable to beam-like structures. This method involves rigorous mathematical derivation using multi-scale analysis to address macroscale and microscale problems. The macroscale level is modelled as an anisotropic Navier–Euler–Bernoulli–Saint-Venant beam [49], while the microscale focuses on a unit cell. The derivation of periodic B.C. for slender beam-like structures has been extensively studied [50–52]. To maintain simplicity, the detailed mathematical derivation is not reiterated in this paper. Interested readers can refer to [51,52] for comprehensive details. Below, we provide the final equations for periodic B.C., their physical interpretations, and their implementation in FEM packages.

The primary goal of this method is to establish a kinematic relationship between the nodes along the same generatrix, as illustrated by Node A and Node B in Fig. 4. Since these two nodes lie on the same generatrix, the line they form is parallel to the neutral axis of the cable. They are paired together and then linked to Node C, located at the midpoint of the left cross section. Node B and Node C form a line that is perpendicular to the neutral axis. This constraint ensures that the degrees of freedom (DOFs) of Node B are constrained, making Nodes A and the master Node C the controlling nodes. Based on the periodic boundary conditions described in [53], the relationship among Node A, Node B, and RP C is as follows:

$$\overrightarrow{C'B'} = \boldsymbol{R}(\boldsymbol{\phi}^C)\overrightarrow{CB} + \overrightarrow{AA'}, \quad \boldsymbol{\phi}^C = [\phi_1^C \ \phi_2^C \ \phi_3^C] \tag{3}$$

Letters without a superscript denote the initial node positions, while those with a superscript indicate the node positions after deformation. The rotation vector of node C is represented by $\boldsymbol{\phi}^C$, and $\boldsymbol{R}(\boldsymbol{\phi}^C)$ denotes the associated rotation matrix. When rotational degrees of freedom (DOFs) are included, such as in the use of beam or shell elements, the relationship is expressed as follows:

$$\boldsymbol{\phi}^B - \boldsymbol{\phi}^A - \boldsymbol{\phi}^C = 0 \tag{4}$$

In a FEM program, the matrices representing derivatives of the constraint function regarding the nodal DOFs need to be provided. Denoting the original coordinates of A, B and C as $\boldsymbol{X}^A$, $\boldsymbol{X}^B$ and $\boldsymbol{X}^C$, respectively, then the coordinate of A′, B′ and C′, the coordinate after deformation, can be described as $\boldsymbol{X}^A + \boldsymbol{U}^A$, $\boldsymbol{X}^B + \boldsymbol{U}^B$ and $\boldsymbol{X}^C + \boldsymbol{U}^C$, respectively. Here $\boldsymbol{U}$ is the translational displacement vector of each node. Therefore, Eq. (3) can be rewritten as:

$$\boldsymbol{X}^{\mathrm{B}} + \boldsymbol{U}^{\mathrm{B}} - \boldsymbol{X}^C - \boldsymbol{U}^C = \boldsymbol{R}(\boldsymbol{\phi}^C)(\boldsymbol{X}^{\mathrm{B}} - \boldsymbol{X}^C) + \boldsymbol{X}^A + \boldsymbol{U}^A - \boldsymbol{X}^A \tag{5}$$

Eq. (5) and (4) can be reorganized as:

$$\boldsymbol{f}_1(\boldsymbol{U}^{\mathrm{B}}, \boldsymbol{U}^{\mathrm{A}}, \boldsymbol{U}^{\mathrm{C}}) = \boldsymbol{X}^{\mathrm{B}} + \boldsymbol{U}^{\mathrm{B}} - \boldsymbol{X}^{\mathrm{C}} - \boldsymbol{U}^{\mathrm{C}} - \boldsymbol{R}(\boldsymbol{\phi}^{\mathrm{C}})(\boldsymbol{X}^{\mathrm{B}} - \boldsymbol{X}^{\mathrm{C}}) - \boldsymbol{U}^{\mathrm{A}} = 0 \tag{6}$$

$$\boldsymbol{f}_2(\boldsymbol{\phi}^{\mathrm{B}}, \boldsymbol{\phi}^{\mathrm{A}}, \boldsymbol{\phi}^{\mathrm{C}}) = \boldsymbol{\phi}^B - \boldsymbol{\phi}^A - \boldsymbol{\phi}^C = 0 \tag{7}$$

For an FEM package to properly handle the equation, it is necessary to supply matrices that represent the derivatives of the constraint function concerning the nodal DOFs [54]. These matrix coefficients are obtained by taking partial derivatives with respect to the displacements of each node. Specifically, for nodes A, B, and C, the relationships are as follows:

$$\boldsymbol{A}^A = \begin{bmatrix} -\boldsymbol{R}(\boldsymbol{\phi}^{\mathrm{C}}) & \boldsymbol{0} \\ \boldsymbol{0} & -\boldsymbol{I} \end{bmatrix} \tag{8}$$

$$\boldsymbol{A}^{\mathrm{B}} = \boldsymbol{I} \tag{9}$$

$$\boldsymbol{A}^C = \begin{bmatrix} -\boldsymbol{I} & \boldsymbol{Q} \\ \boldsymbol{0} & -\boldsymbol{I} \end{bmatrix} \tag{10}$$

where $\boldsymbol{Q} = -\partial \boldsymbol{R}(\boldsymbol{\phi}^{\mathrm{C}})(\boldsymbol{X}^{\mathrm{B}} - \boldsymbol{X}^{\mathrm{C}} + \boldsymbol{U}^{\mathrm{A}})/\partial \boldsymbol{\phi}^{\mathrm{C}}$. When rotational DOFs are included in the model, such as with beam or shell elements, the three matrices are 6 × 6. If only translational DOFs are considered, the last three rows of these matrices can be omitted. To determine $\boldsymbol{A}^{\mathrm{A}}$ and $\boldsymbol{A}^{\mathrm{C}}$, it is essential to provide $\boldsymbol{R}(\boldsymbol{\phi}^C)$.

A computationally efficient and convenient method to handle finite rotations, particularly in the presence of compound rotations, is through the use of quaternion parameters [55]. Quaternions are a mathematical tool extensively applied in 3D computer graphics, robotics, and physics for representing rotations and orientations. They offer greater numerical stability, help avoid gimbal lock problems, and provide a concise and efficient representation of 3D rotations.

Quaternion can be expressed by the combination of a scalar $q_0 \in R$ and a vector field $\boldsymbol{q} \in R^3$:

$$q = (q_0, \boldsymbol{q}) = q_0 + \boldsymbol{q} \tag{11}$$

where q_0 and $\boldsymbol{q}$ are respectively defined as:

$$\begin{cases} q_0 = \cos(\phi/2) \\ \boldsymbol{q} = \sin(\phi/2)\boldsymbol{n} \end{cases} \tag{12}$$

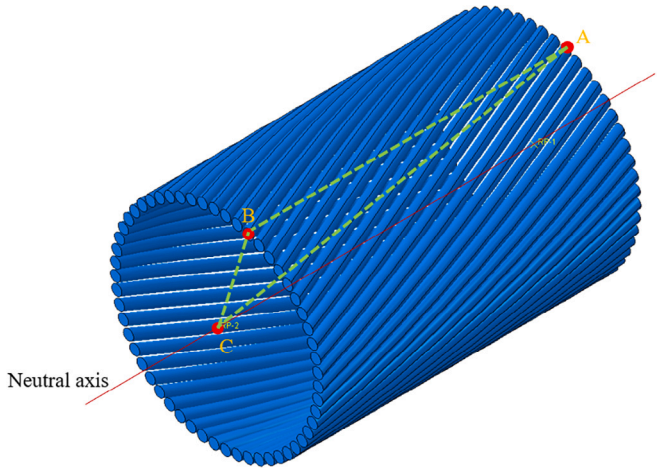

Fig. 4. Nodes involved in periodicity conditions on the helical components.

In terms of the four quaternion parameters q_0 and $\boldsymbol{q}$ the rotation matrix $\boldsymbol{R}$ takes the homogeneous quadratic form:

$$\boldsymbol{R} = (q_0^2 - \boldsymbol{q}^T\boldsymbol{q})\boldsymbol{I} + 2q_0\hat{\boldsymbol{q}} + 2\boldsymbol{q}\boldsymbol{q}^T \tag{13}$$

$\hat{\boldsymbol{q}}$ is the skew-symmetric matrix with axial vector $\boldsymbol{q}$. The corresponding component representation is:

$$R_{ij} = (q_0^2 - q_k q_k)\delta_{ij} - 2\epsilon_{ijk}q_0 q_k + 2q_i q_j \tag{14}$$

In full matrix form, the rotation representation is:

$$\boldsymbol{R} = \begin{bmatrix} r_0^2 + r_1^2 - r_2^2 - r_3^2 & 2(r_1r_2 - r_0r_3) & 2(r_1r_3 + r_0r_2) \\ 2(r_1r_2 + r_0r_3) & r_0^2 - r_1^2 + r_2^2 - r_3^2 & 2(r_2r_3 - r_0r_1) \\ 2(r_1r_3 - r_0r_2) & 2(r_2r_3 + r_0r_1) & r_0^2 - r_1^2 - r_2^2 + r_3^2 \end{bmatrix} \tag{15}$$

The coefficients in Eqs. (8) and (10) can thus be obtained.

Since this model is designed to handle not only single-core SPCs but also three-core SPCs and other multi-core SPCs, the guidelines for determining the model length for these various types of SPCs need to be standardized. The requirement for the model length is as follows:

$$l = k\frac{p_i}{m_i} \tag{16}$$

where $k \in \mathbb{N}$, p is the pitch length, m is the number of helices, and the index i represents the sequence of the current layer. For a single-core SPC, the helical components are present only in the armour layers, with all inner components being straight. Thus, the model length is determined solely by the pitch lengths and the number of wires in the armour layers. In contrast, for a multi-core SPC, the inner components are also helical, which also gives a model length based on Eq. (16). The final model length is decided by the least common multiple of the lengths of the armour layers and the inner helical components. Typically, the inner helical components dictate this value because their m, the number of helical components, is relatively small, and their pitch length is normally larger. For instance, $m = 3$ for the inner helical components in a three-core SPC. In any case, the calculated model length is shorter than the model with one pitch length of the inner components.

The solution to the periodic boundary conditions is akin to three-body movements with specific internal constraints, which can induce rigid body displacements [56]. To counteract the effects of these rigid body displacements, additional constraints on the structure are necessary. Unlike the method used by Tyrberg [16], which involves adding a viscous damping coefficient and requires the ratio of damping energy to total strain energy to be less than 5% at the simulation's end, this paper proposes an alternative boundary condition (B.C.) to eliminate the damping effect from rigid body movement. This unified B.C. is easily applicable to both single-core and multi-core SPCs. The unified B.C. for single-core and three-core SPCs is depicted in Fig. 5.

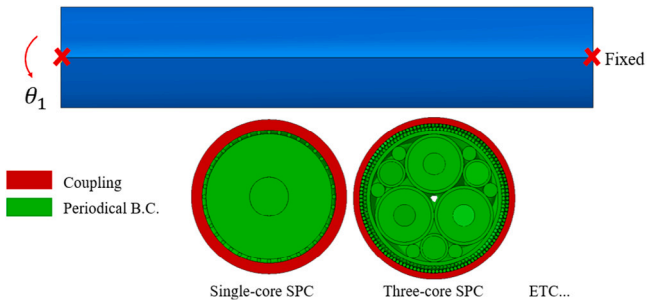

Fig. 5. The illustration of the boundary conditions for SPCs under bending.

The outer PE cylinder on both ends is coupled with a reference point (RP) located at the centre of its respective cross-section. All other components on both sides are constrained by the periodic boundary conditions. The right RP is fixed, while the loadings are applied on the left RP. In this way, the rigid body movement is eliminated by the constraints on the outermost PE layer. Besides, the B.C. for other multi-core SPCs can also be set up similarly. Since this model is based on periodic boundary conditions applied to a repetitive unit cell (RUC), it will be referred to as the RUC model for clarity in the following discussion.

3. Tests

A core of this paper is the validation of the RUC model under bending, accomplished after obtaining the data from the bending test regarding single-core SPCs and a three-core SPC, whose cross section is presented in Fig. 6. Fig. 7 shows clearly how the tests work during the calibration and validation process. The curvature–bending moment curves from the single-core SPC test aim to calibrate the damping coefficient that will be input into the RUC model of the three-core SPC. Finally, the curvature–bending moment curve from the bending test regarding the three-core SPC will be used to validate the RUC model.

Bending tests regarding the single-core SPC and the three-core SPC are given in the following two subsections, respectively. The configurations of test facilities and the test process are described in detail. Curvature–bending moment curves of the two types of SPCs are the core outputs from the tests.

3.1. Bending tests of the single-core SPC

Fig. 8(a) shows the cable samples that were used in the bending test. Their lengths are 600 mm. The geometry size of the samples in the length direction is shown in Fig. 8(c). They were then placed on a four-point bending test facility with two supports to hold the cables and two loading rings to apply the bending on them, as shown in Fig. 8(b). Three displacement sensors are installed below the cable, and then the displacements of these three points could be captured for calculating the curvature. The bending results are given and discussed in Section 4.

3.2. Bending test of the three-core SPC

Fig. 9(a) shows the three-core SPC sample that was used in the bending test. It has a length of 9 m. The geometry size of the samples in the length direction is shown in Fig. 9(b). The sample was bent manually several times before the bending test to make the inner components contact as much as possible. They were then placed horizontally on a four-point bending test facility to avoid the influence of gravity. The facility has two supports to hold the cables and two loading rings to apply the bending on them. Three displacement sensors

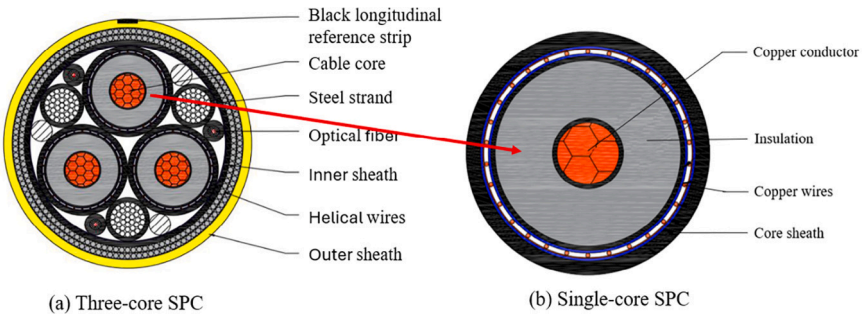

Fig. 6. The cross sections of the SPCs.

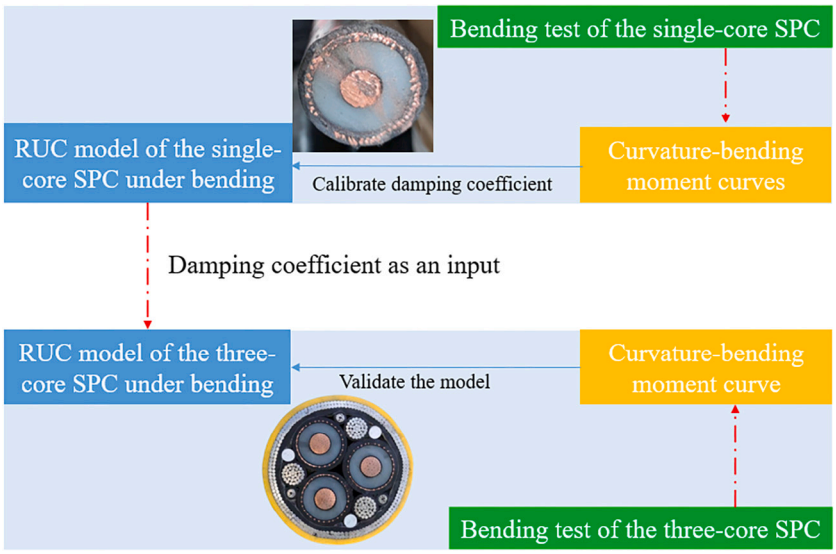

Fig. 7. The calibration and validation flow chart.

were installed on the loading rings and the middle of the cable to record the displacements of the corresponding three nodes. Meanwhile, the loadings applied by the two loading rings were also recorded. The curvature of the cable and the moment applied to it can then be calculated. The loading rings can bend the cable in one direction and then bend it back to its original place; therefore, in this way, the curvature of the cable increased first and decreased back to zero at last.

4. Validation of RUC model under bending

As mentioned, the influence of the initial residual stress within the SPC can be dealt with by applying damping among the contact interfaces. However, the damping coefficient is unknown and needs to be calibrated through test results. In this part, the curvature–bending moment curves from the single-core SPC test are set as the calibration benchmark, and then the value of the calibrated damping coefficient is inputted into the three-core SPC model, which outputs the curvature–bending moment curve that is validated by the test data from the three-core SPC test. The calibration and validation flow chart is already shown in Fig. 7. The constructions of the RUC model of the single-core SPC and the three-core SPC are presented first.

4.1. Construction of the two types of SPCs

The geometries of the three-core SPC model and the single-core SPC model are presented in Fig. 10. The RUC model for the single-core SPC is 40 mm, while the one for the three-core SPC is 792 mm, according to Eq. (16).

All the contact interactions among each component are taken into account. Surface-to-surface discretization method is used to model the contact between surfaces where both the tangential behaviour and normal behaviour employ the penalty method. The friction coefficient provided by the cable manufacturer is 0.3. The normal contact is set as the default hard contact. Different than in the tension case, contact damping coefficient is set upon all the contact surfaces in the bending case, and the value will be calibrated by the curvature–bending moment curves from the bending test regarding the single-core SPCs.

Before the calibration, the soundness of the beam plus surface elements under the bending case also needs to be verified first without damping introduced yet. The model built with all solid elements is termed Case-1, while the other one built with beam plus surface elements is termed Case-2. In the three-core SPC, the components that employ beam plus surface elements include copper conductor, helical strands and all the helical wires. The mesh convergence studies were performed on both the single-core SPC and the three-core SPC in the same manner. Convergence was achieved by checking the curvature–bending moment curves from the simulation results. First, the mesh number in the axial direction of the cable was adjusted until convergence was obtained with an appropriate mesh density. Second, the mesh number of the cable cross-section was assigned using the automatic mesh tool in ABAQUS/Standard with the dynamic implicit algorithm [34]. We adjusted the mesh number of the cross-section until convergence was obtained. Finally, the mesh densities in the axial direction and the cross-section, confirmed by the previous two steps, were utilized throughout the simulation. The mesh results of the three-core SPC in these two ways are already shown in Fig. 11(a) and Fig. 11(b), respectively.

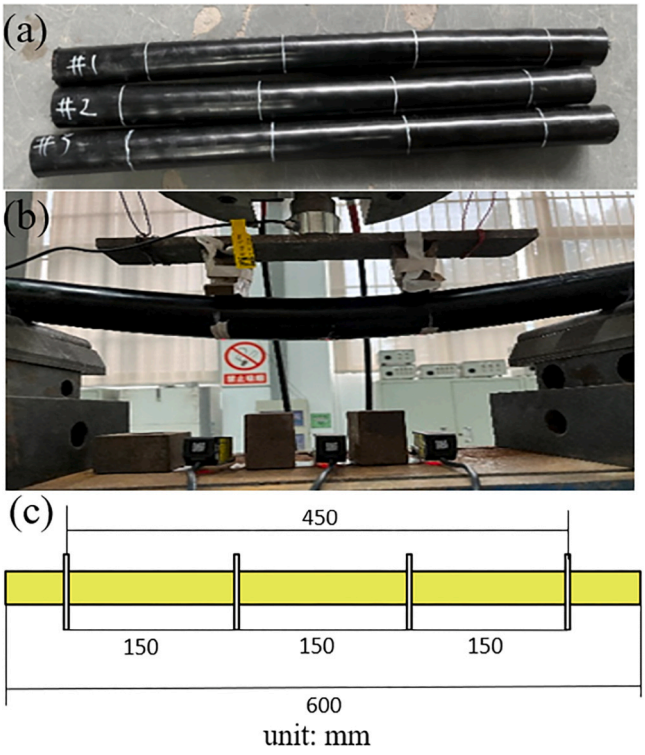

Fig. 8. The cable samples (a), the four-point bending test (b) and the dimensions (c).

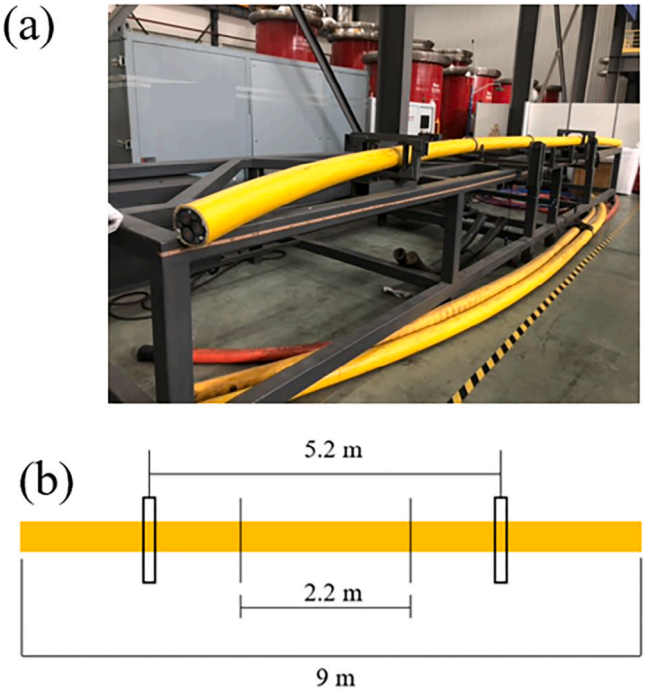

Fig. 9. Test of three-core SPC (a) and the dimension of the specimen (b).

All models were run on the DelftBlue Linux supercomputer [57] with 16 cores. The calculation time of Case-2 is found to decrease from 90.6 h to 5.3 h, which is around 17 times more efficient than Case-1. The reliability of the beam plus solid technique is verified by comparing the curvature–bending moment curve from both models, as shown in Fig. 12. The cable has an outer diameter of 149.6 mm. Due to commercial confidentiality, the other data in this paper has been normalized. The information of both models is listed in Table 2 for reference. The overall curvature–bending moment from both models is quite near, with an error of 2.0%. Therefore, for the consideration of the model efficiency, the following analysis will rely on Case-2.

Table 2
The information of the two types of RUC model.

	Case-1	Case-2
Element types	Solid	Solid & beam & surface
Number of elements	3 150 320	1 588 208
Number of nodes	6 276 347	2 905 591
Cost time	90.6 h	5.3 h

4.2. Calibration of the damping coefficient

The curvature–bending moment curves of the single-core SPCs from the test are presented in Fig. 13(a). Notice, the curves are normalized according to the maximum curvature and the maximum bending moment the three-core SPC bears in the test. The maximum curvature applied in the single-core test is nearly ten times larger than that in the three-core bending test. Some of the materials in the single-core SPC sample will enter their plasticity if the curvature is larger than a specific value, and the conductor will not keep as an entirety; therefore, the curve gradually shows more nonlinear variation. This deformation has violated the assumption of simplifying the copper conductor into a solid cylinder. As the curvature considered in the three-core bending test is less than 1, there is no need to consider the deformation when the curvature is larger than 1. Only the curves corresponding to a curvature less than 1 are extracted and processed averagely for the single-core SPC as well.

The curve after the average and fitting process is presented in Fig. 13(b) for the purpose of calibration. It is observed that the curve is composed of two lines, although the first line is not so obvious in the image. This curve also demonstrates that there are stick–slip issues within the single-core SPC. After slippage, the bending stiffness, i.e., the slope of the curve, becomes smaller. It is worth mentioning at this juncture the bending moment contributed by the single-core SPC is only near 0.6% of the overall three-core SPC when curvature = 1, demonstrating that the three cores are not the main contribution to the overall bending behaviour in the three-core SPC. Therefore, for an efficient calculation of the three-core SPC model, the armour wires in the single-core SPC can be merged into the neighbouring layer. This simplification has a minor influence on the overall behaviour but saves many calculation resources.

A sensitivity study on the damping coefficient is performed on the single-core SPC. The damping coefficient is kept the same throughout the simulation process. Four cases are studied with values varying from 0 to 3 with an increment of 1. The simulation results, together with the test result, are shown in Fig. 14. The curvature–bending moment curves after damping incorporated into the model are basically composed of two lines corresponding to the stick and slip phases. The stiffness before the slip appears is termed stick stiffness, while the one after the slip is termed slip stiffness. With an increase in the damping coefficient, the stick curve becomes longer, which means the slippage appears later; the bending moment predicted by the model becomes larger, while the slip stiffness does not change significantly. The materials within the single-core SPC under such curvature range are basically within their elastic phase. The simulation curve best fits the test result when the damping coefficient equals 1. Therefore, this calibrated value will be inputted into the three-core SPC for validation.

4.3. Validation of the RUC model under bending

Subsequently, the calibrated damping coefficient is inputted into the RUC model for the three-core SPC. A cyclic bending is applied

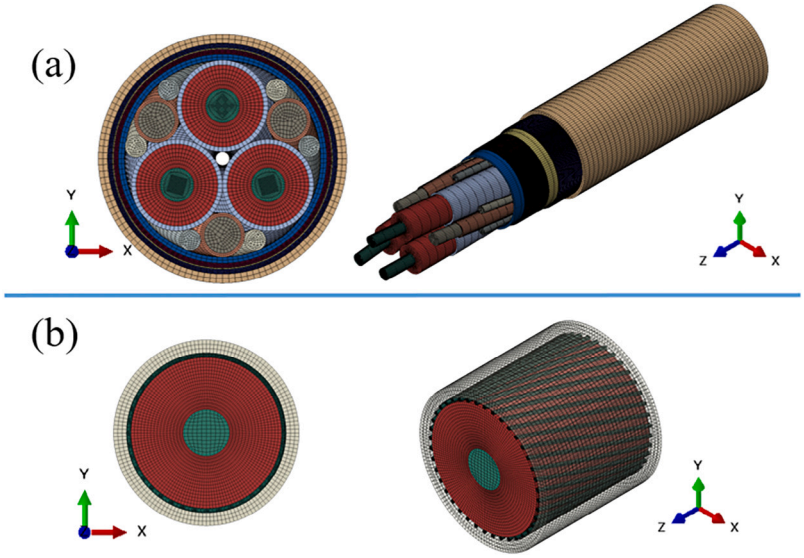

Fig. 10. The RUC model of the three-core SPC (a) and the single-core SPC (b).

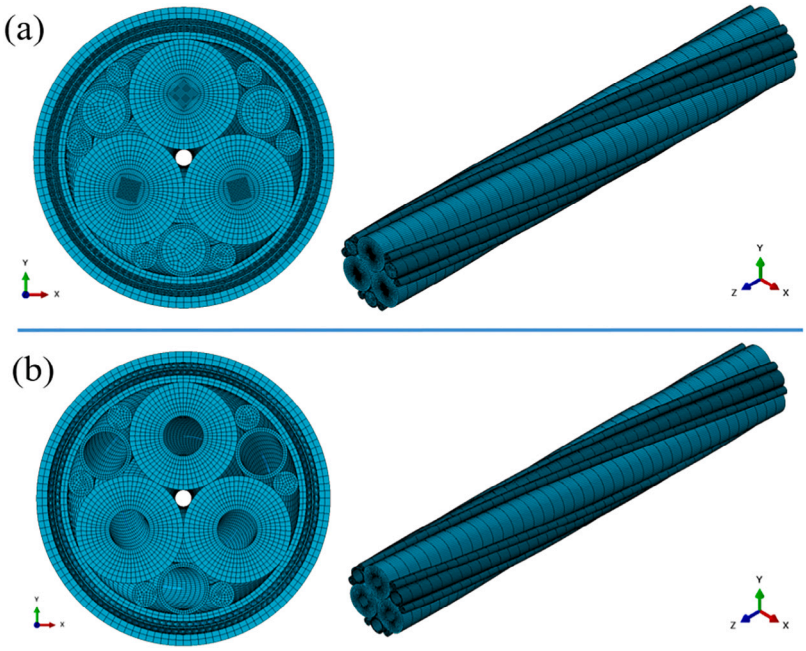

Fig. 11. Mesh of the three-core SPC by using solid elements (a) and beam & surface elements (b).

on the RUC model where the variation of bending angle θ is illustrated in Fig. 15. The time in this figure is for the convenience of the elaboration of the following content where 't' appears frequently and corresponds to the 't' here in this image. A sensitivity study of the damping coefficient on the bending behaviour is performed. The damping coefficient changes as 0, 0.5, 1 and 2. The curvature–bending moment curves from the four cases are presented in Fig. 16. When the damping coefficient equals 0, again it is found that no stick–slip curve is predicted. This is because the components immediately slip away from each other within the SPC. The classical hysteresis curve can be obtained after inputting the damping coefficient into the RUC model. When the damping coefficient equals 1, i.e., the value calibrated from the single-core SPC bending test, the simulation result agrees the best with the test result.

When the damping coefficient equals 1, the curvature–bending moment curves from the simulation and the test are shown in Fig. 17. There are two sections of stick stiffness and two sections of slip stiffness from the test curve. They are named stick stiffness-1, stick stiffness-2, slip stiffness-1 and slip stiffness-2, respectively. The fitting curves of these stiffnesses are shown in Fig. 17, and their values are given in Table 3. In the test results, it is observed that there is a difference between stick stiffness-1 and stick stiffness-2, which is also the same situation for the two slip stiffnesses. This might be caused by the operation during the test and the complication of the cable cross section. The cable sample will become stabler after several cyclic bending, and their stiffnesses will tend to stable values. The slip stiffnesses in the loading process and unloading process from the RUC model, however, tend to be close to each other. The stiffnesses during the unloading process from the test are more reliable because the cable sample became stabler after the first loading process; therefore, it is found that the stick stiffness and slip stiffness during the unloading process from the test and the RUC model agree with each other quite well, with an error

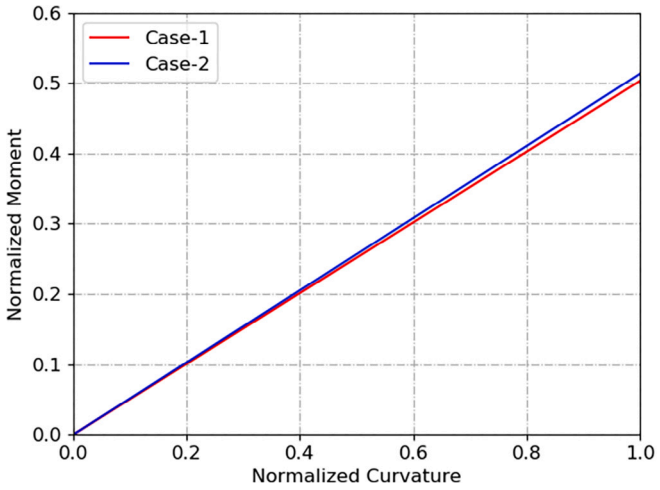

Fig. 12. The curvature–moment curves from the two RUC models.

Table 3
The stiffness from the test and RUC model.

	Test	RUC model	Error
Stick stiffness-loading	8.41	7.01	16.6%
Slip stiffness-loading	0.55	0.74	25.7%
Stick stiffness-unloading	6.86	6.71	2.2%
Slip stiffness-unloading	0.79	0.75	5.1%

of 2.2% and 5.1%, respectively. The values of the stiffness from both methods after the fitting process are listed in Table 3.

5. Full-scale models

In order to verify the efficiency of the RUC models, full-scale models of the single-core SPC and the three-core SPC are built. The full-scale models here refer to the numerical models not based on periodical boundary conditions. The lengths of the full-scale models cannot be reduced by taking advantage of the helical configurations of the components, which makes their lengths longer. Their details are given below.

5.1. Construction of the full-scale models

It is extremely difficult to simulate the bending process by building the model exactly like that in the test, i.e., the four-point test condition, as this will cost too much calculation resources and thus not realistic under current computation capability. Therefore, the full-scale models have to be simplified in a way that balances accuracy and calculation efficiency. However, there is scarce guidance on how to set up the appropriate boundary conditions for the pure-bending section of a four-point bending test sample, and so is the case for the specific rules on the requirement of the model length. Here the boundary conditions under two extreme conditions are tested, i.e., one with all the components on both sides coupled with the corresponding RPs, termed B.C.-1, and the other one with only the PE materials coupled with the corresponding RPs, named as B.C.-2. They are shown in Fig. 18. The first one corresponds to the situation where all the components on both sides are restricted, while the second one enables the movement of the metals within the cable more freely without any boundary constraints but only with the constraints from the neighbouring layers, Two opposite bending angles are applied on the RPs to simulate the pure-bending section. The full-scale model of the single-core SPC has a length of 400 mm, equalling one pitch length of the helical wires and also meeting the requirement given by Paumier [58], who claimed that the model length is supposed to be 5 times longer than its diameter in a flexible pipe. The full-scale model of the three-core SPC has a length of 2376 mm, which equals one pitch length of the component with the maximum pitch length in the structure.

Table 4
The information of the RUC model and the full-scale model.

	Full-scale model (B.C.-1)	Full-scale model (B.C.-2)	RUC model
Length	2376 mm	2376 mm	792 mm
Number of elements	4 745 288	4 745 288	1 588 208
Number of nodes	8 642 538	8 642 538	2 901 751
Cost time	70 h	70 h	5.3 h

5.2. Discussions

The curvature–bending moment curves from the two full-scale models, as well as the fitting curve from the test regarding the single-core SPC, are presented in Fig. 19. Unlike the test curve, the simulation curves from both models are composed of only one straight line, which does not represent the stick–slip phenomenon. It is also found that the moments from both simulation curves are lower than those from the test curve. The reason is that the initial residual stress has not been considered in current models. A similar phenomenon will be found in the following simulation results on the three-core SPC as well. To deal with this issue, the initial residual stress also needs to be taken into account.

The curvature–bending moment curves from the two full-scale models and the curve from the test regarding the three-core SPC are presented in Fig. 20. The process of the SPC's reversing back is not simulated by the full-scale model considering the calculation cost. The same as the situation in the single-core case, in the three-core case, it is observed that, unlike the test curve, the simulation curves from both models are composed of only one straight line. The stiffnesses from both models are less than the stick stiffness from the test result. This is also because current models do not consider the initial residual stress within the SPC. Thus the components immediately slip after loaded, and the stick–slip issue does not appear. The friction force is determined by the friction coefficient and the normal stress of a contact interface. The lack of normal stress in current models enables the slippage instantly when a bending is applied. Therefore, for a more realistic representation of the mechanical behaviour of the SPC under bending, the full models also show that initial residual stress has to be taken into account in a reasonable way.

6. Mechanical analysis of the SPC under bending

The RUC model has been validated by the test results. Then the mechanical behaviour of the components can be studied based on this model, from the overall level and component level. The focus is on the three-core SPC as it is the final form after all the components, including the single-core SPCs, are assembled.

6.1. Cable overall behaviour

Fig. 21 presents the curvature–bending moment curves from the experiment, the RUC model and two full-scale models with the same damping coefficient calibrated by the single-core SPC test. These two full models have the same boundary conditions as those of B.C.-1 and B.C.-2 in Section 5.1. The calculation times of the two models are summarized in Table 4. The cost time regarding the RUC model is recorded when it stops at t = 1 s, and the cost time is 5.3 h. The full-scale models stop before t = 1 s, yet their cost time has already reached 70 h.

Due to the differences regarding the boundary conditions between the full-scale models and the RUC model, their curves still have differences even when the length of the full-scale model is prolonged to

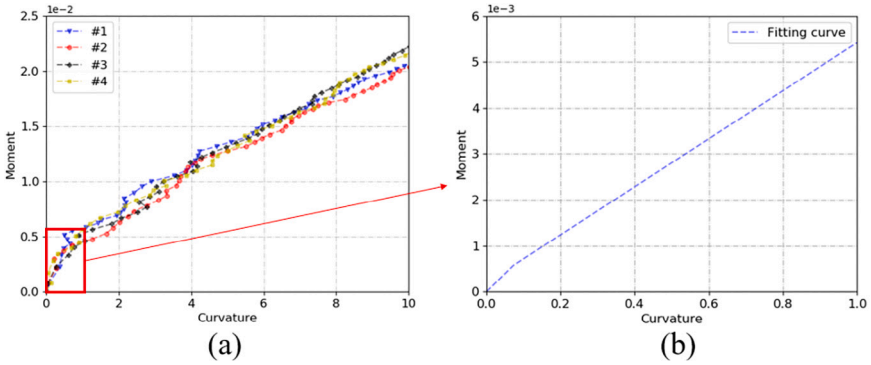

Fig. 13. The test results of the single-core SPC (a) and the curve after average and fitting (b).

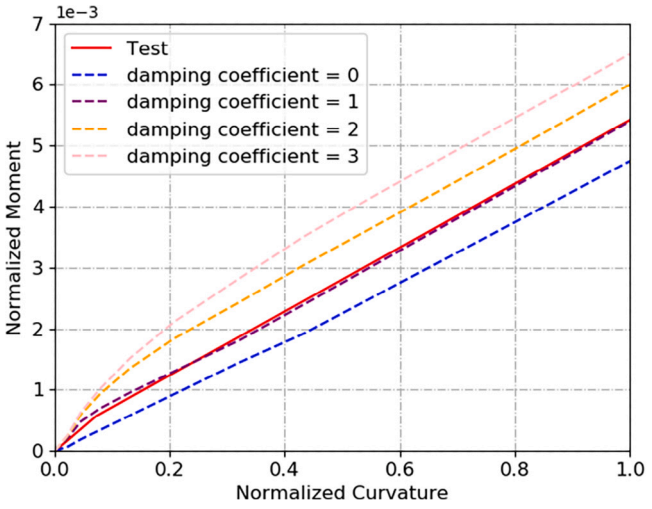

Fig. 14. The influence of damping coefficient on the curvature–bending moment curves of the single-core SPC.

2376 mm. It is found that the curve from the RUC model is sandwiched between the curves from Full-scale model-1 and Full-scale model-2, regarding both their stick stiffnesses and slip stiffnesses. This can be well explained by their boundary differences. All the components on both sides in Full-scale model-1 are coupled, which is an extreme situation as both cross sections are constrained. However, in Full-scale model-2, only the PE components are coupled, and the contributions from the metals are only propagated to the coupled RP through the contact within the interfaces. As compared to the full-scale models, the RUC model predicts the stiffnesses closer to the test results overall as the RUC model is proposed to deal with a structure with infinite length where the boundary effects are eliminated as much as possible. Therefore, the RUC model performs better than the full-scale models in terms of both efficiency and accuracy. The following analysis will rely on the RUC model.

The appearance of the stick–slip point in the curvature–bending moment and the stick–slip phenomenon strongly involve the energy dissipation in the structure; therefore, the energy variation during the simulation process is of interest. Five types of energy variation, frictional dissipation, viscous dissipation, plastic dissipation, internal energy and kinetic energy, throughout the simulation process from the RUC model, are outputted and presented in Fig. 22. First, the kinetic energy during the process is extremely small, illustrating that the dynamic effect can be ignored. The second large energy is the plasticity dissipation energy, which gradually increases after several cyclic bendings in the RUC model but is still quite small. This also explains why the curve corresponding to 0- 1 s does not coincide with

Table 5
The predicted bending stiffnesses of the models with different friction coefficient.

	Stick stiffness-loading	Slip stiffness-loading
Friction = 0	7.01	0.70
Friction = 0.1	7.01	0.72
Friction = 0.2	7.01	0.73
Friction = 0.3	7.01	0.74
Friction = 0.4	7.01	0.75

the curve corresponding to 4–5 s in Fig. 17. The internal and plastic dissipation energy within the SPC vary throughout the process; thus, the curvature–bending moment curve is not always the same after a bending cycle, which should be paid attention to in practice. Although the frictional dissipation becomes more obvious than the plastic dissipation, it is not the dominant factor to cause the loss of energy in the model. Rather, the viscous dissipation due to the contact damping is found to be much larger than the other energy types, illustrating its major influence on the mechanical behaviour of the SPC. This is exactly why the overall mechanical behaviour is obviously affected by the damping coefficient in Fig. 16. A sensitivity study on the friction coefficient is also performed, given below.

Their corresponding curvature–bending moment curves of five RUC models under different friction coefficients are presented in Fig. 23. It is found that all of the curves basically overlap. This can also be explained by the energy variation in Fig. 22. The friction dissipation in the model under these situations is not the main factor in affecting the overall mechanical behaviour, instead, the viscous dissipation caused by the damping is the dominant factor. Even if the friction coefficient changes from 0 to 0.4, the stick stiffness basically has no change; the slip stiffness only has an error of 6.7%, as summarized in Table 5. In order to check how stresses are distributed within the cable, and how the inner components behave, an analysis on the component level is given below.

6.2. Cable component behaviour

As the inner components are arranged in the inner sheath helically with gaps, the pressure does not distribute uniformly along the sheath after bending is applied. As shown in Fig. 24, when t = 1 s, CPRESS, i.e., the contact pressure, has a specific pattern according to the helical shapes of the inner components. To investigate how the contact pressure distributes around the cross-section of the inner sheath, a middle section is cut out, as shown in Fig. 24(b). Then the contact pressure of the inner sheath at this cross-section when t = 1 s, t = 2 s and t = 3 s is outputted and shown in Fig. 25. Point B, point F and point J are the contact points between the three cores and the inner sheath, as defined in Fig. 26.

From Fig. 25, it can be found that the maximum contact pressure appears at the contact point between the inner sheath and the inner

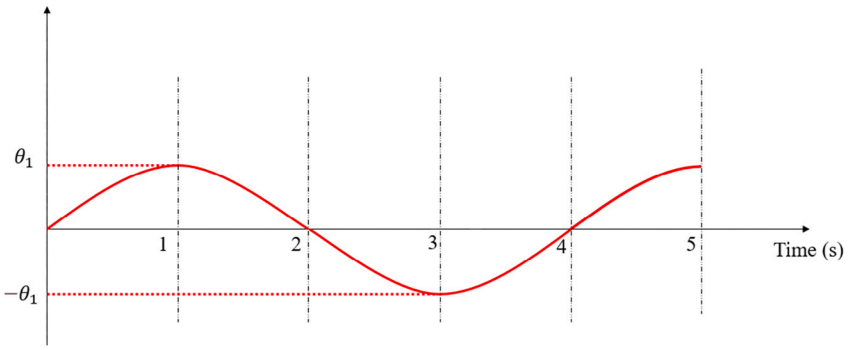

Fig. 15. Loading strategy for cyclic bending of the three-core SPC.

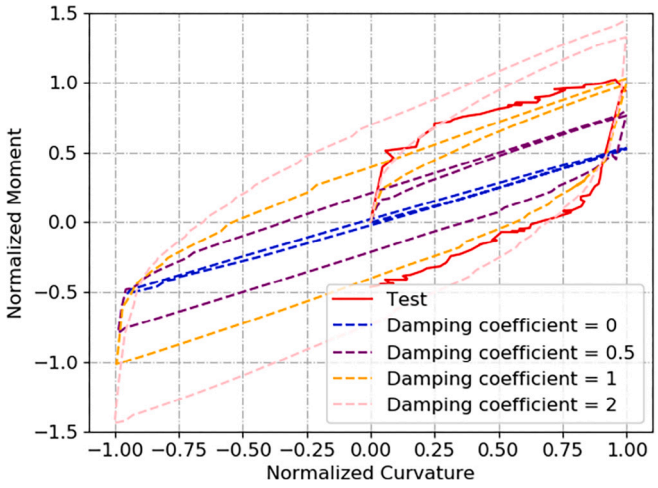

Fig. 16. The sensitivity study of the damping coefficient on the three-core SPC.

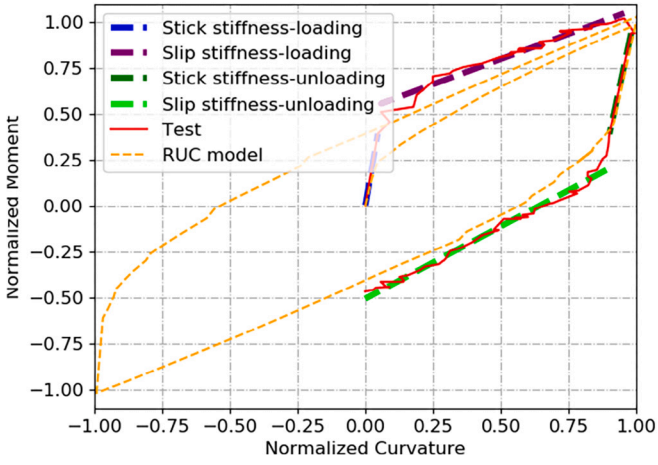

Fig. 17. Curvature–bending moment for the three-core SPC from RUC model.

components, while the areas with no contact do not have any pressure. When t = 1 s and 2 s, the maximum contact pressures are located at point B, point F and point J. However, when t = 3 s, the SPC has been bent into the reverse direction, the locations of the three peak locations are no longer the same. The uneven contact pressure throughout the bending process will also cause uneven stress on the components, which will be investigated below.

When t = 1 s, a bending moment has been applied on the SPC that achieves the highest curvature. The stress distribution among the components is one of the design parameters that cable designers care about. Fig. 27 presents the stress distributions of the cross-section of the whole cable and all the PE layers. It can be found that the metals in the SPC, including the steel strand, helical wires and conductors, bear much of the stresses. As Young's modulus of the material steel is much higher than that of the material copper, the stress of the former is also much higher than that of the latter. In addition, the stresses of the inner steel strands are also higher than those of the helical wires in the armour layers. These steel strands are put into the SPC to bear those harsh loadings together with the armour layers. As fatigue has also been reported for the armour layer, this special design reduces the stresses in the helical wires and then increases the performance of the SPC. From Fig. 27(b), the maximum stress the PE materials withstand is only 3.91 MPa, with most part of the PE materials staying in their elasticity phase, which justifies the assumption that PE materials can be regarded as elastic in almost all of the previous studies [15,59]. As the metals have fatigue risk in practice, their stresses along the cable are of interest and are extracted for a detailed analysis.

The axial stresses of the metals when t = 1 s, i.e., the time when the highest curvature is applied, are plotted in Fig. 28. The nomination of the three steel strands and three copper conductors are illustrated in Fig. 29. As there are numerous helical wires in two armour layers, and the axial stresses of these wires are distributed unevenly due to the uneven pressure, only four wires in each layer are taken out for illustration purposes. Their starting positions correspond to $V = 0°$, $V = 90°$, $V = 180°$ and $V = 270°$ in Fig. 26.

From Fig. 28, it can be observed that the axial stresses of the inner metals are not disordered like those of the helical wires. The steel strands obviously bear more stress than other metals. Steel strand-3 has only tension stress as it is located on the upper part of the cable, which is tensioned after the bending when t = 1 s. However, the other two steel strands bear not only tension stress but also compression stress. A similar phenomenon is also observed regarding the conductors. Even though the stresses of the helical wires are disordered, one thing that can be observed is that the outer armour layer bears less stress than the inner armour layer. In addition, the helical wires in the armour layers still have much potential, for their stresses are still quite small compared to those from the steel strands and conductors. This can be improved by modifying the configurations of these helical wires. Noteworthy, the stresses of most parts of the metals are within their yield strength, which is realized by the helical design that allows the slippage among components.

The points on helical strands and copper conductors that bear the highest tension and compression stresses are of special interest. They are named as S1, S2, C1 and C2 for the steel strands and copper conductors, as the points illustrated in Fig. 28. Then the stress variations of the four points along with loading time are presented in Fig. 30. Similar variation patterns are found for the four points. Take S1 as an example, when the SPC is bent in one direction, the stress of this point increases until t = 1 s. Then the SPC is bent back to the original location, and the stress decreases to 0 until t = 2 s. Afterwards, the SPC is still bent in the opposite direction and the stress becomes negative, illustrating this point is under compression, and so on.

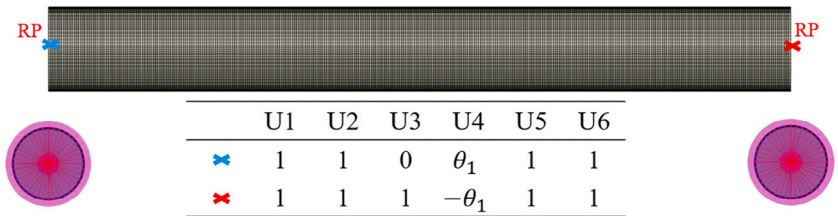

	U1	U2	U3	U4	U5	U6
✖	1	1	0	θ_1	1	1
✖	1	1	1	$-\theta_1$	1	1

1 is fixed and 0 is free

Fig. 18. The boundary conditions for the full-scale model.

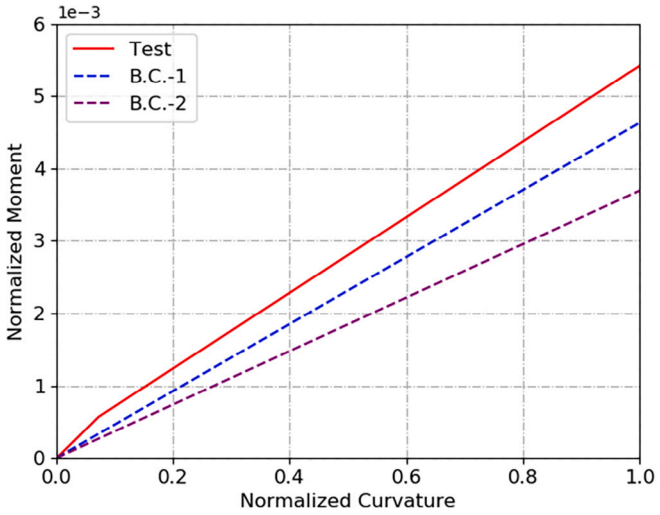

Fig. 19. The test results and the simulation results under two boundary conditions of the single-core SPC.

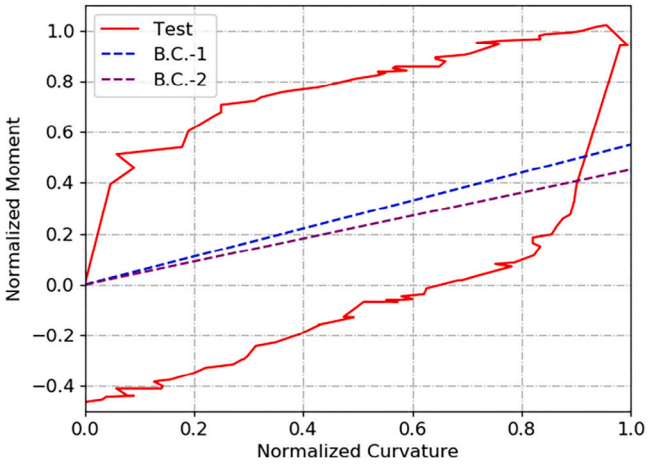

Fig. 20. The curvature–moment curves from the models under two different boundary conditions.

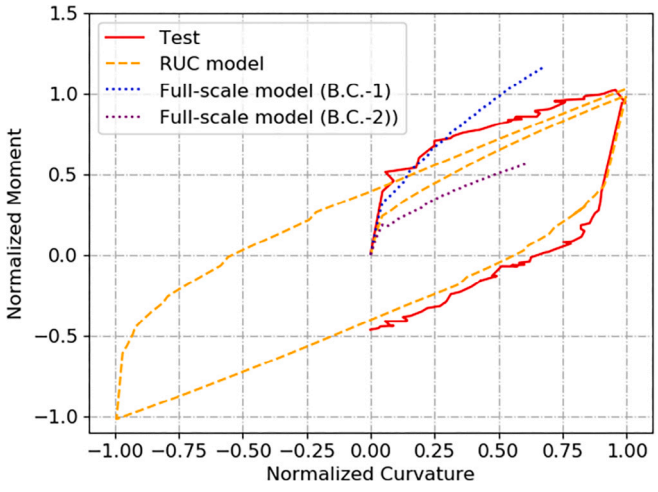

Fig. 21. Overall behaviours from all the methods.

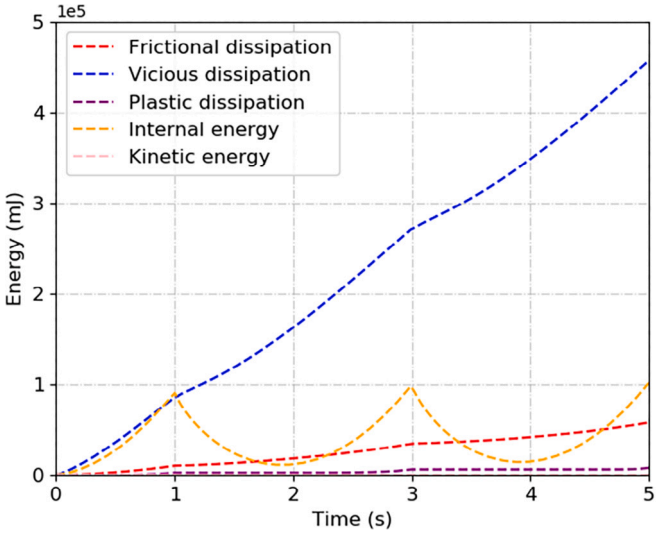

Fig. 22. The variation of the plasticity dissipation and the internal energy throughout the bending based on RUC model.

7. Conclusions

In this study, the Representative Unit Cell (RUC) model has been enhanced to incorporate bending scenario. Initially, the RUC model's bending simulations were validated through bending tests conducted on single-core and three-core submarine power cables (SPCs). Following successful validation, full-scale models featuring two different boundary conditions were constructed for in-depth analysis. Comparative assessments revealed that the RUC model significantly surpasses the full-scale models in accuracy and efficiency, achieving a minimum efficiency improvement of 15 times over the full-scale models we already simplified. Subsequent to the validation phase, detailed mechanical analyses of the three-core SPC subjected to bending were performed, leading to key insights:

(1) The initial residual stress dominates the time that slip appears, as well as the corresponding bending moment. The initial residual stress should be carefully calibrated by the test curve.

(2) The friction coefficient hardly affects the overall bending behaviour after damping is incorporated into the model; thus, this value does not need to be provided by cable manufacturers.

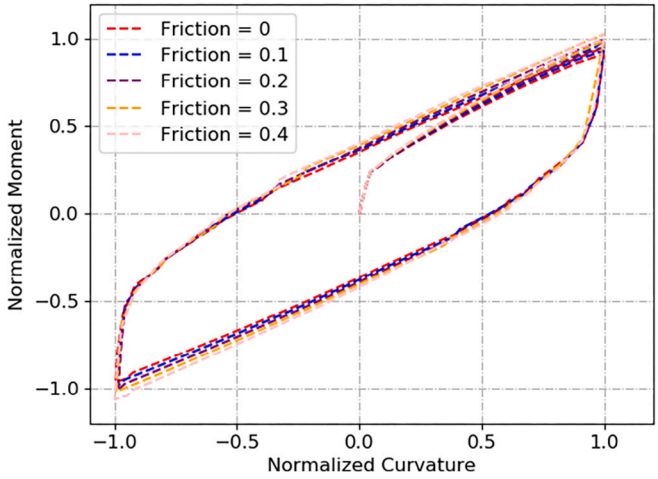

Fig. 23. Curvature–bending moment curves of models with different friction coefficients.

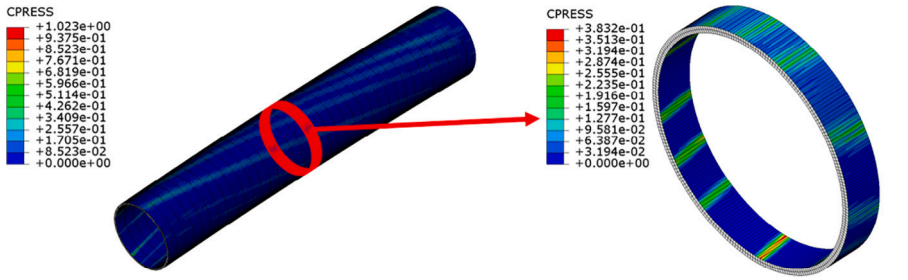

a. Contact pressure along the inner sheath b. Contact pressure of the middle section

Fig. 24. Contact pressure of the inner sheath when t = 1 s.

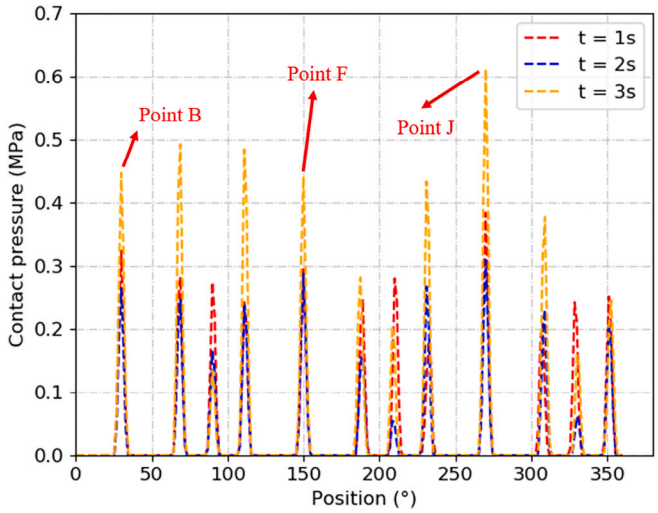

Fig. 25. Contact pressure along the cross section.

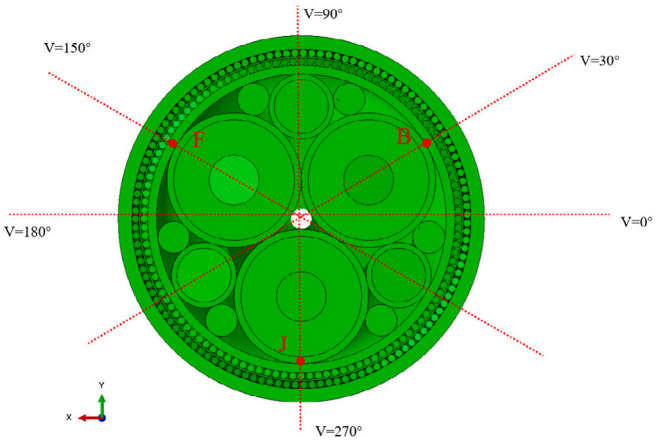

Fig. 26. Illustration of the nodes in the middle cross-section of the three-core SPC.

(3) The metals within this SPC sample are the main components that withstand stress when the cable is under bending. The inner steel strands have the largest stress, followed by copper conductors and then armour layers for this particular cable.

(4) The stresses of both armour layers are uneven without specific order, which is caused by the uneven contact pressure during the bending process. The inner armour layer bears more stress than the outer armour layer does. Besides, there is still much potential in both armour layers, which should be taken advantage of during the design.

(5) The yield of the metals is an important factor in causing the plasticity dissipation in the model. Cable engineers should pay more attention to the inner metals as they already entered plasticity; however, the wires in both armour layers still have much potential.

Furthermore, the RUC model holds much potential in dealing with other loadings, such as torsion, pressure, combined tension and pressure, etc. More test data should be used to validate the RUC model under other loadings. Besides, the thermal effect induced by electricity can also be taken into account by further developing the model. In other words, different physical fields can be integrated into the model, and multi-physical analysis can be performed.

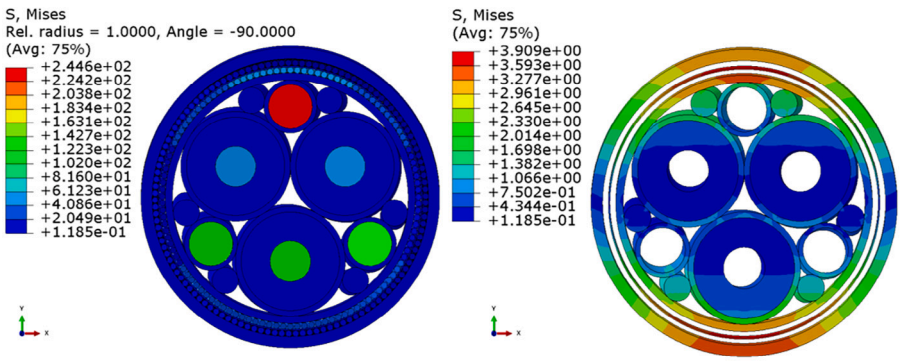

a. All the components in the middle cross section b. All the PE material in the middle cross section

Fig. 27. The stress distribution of the SPC when t = 1 s.

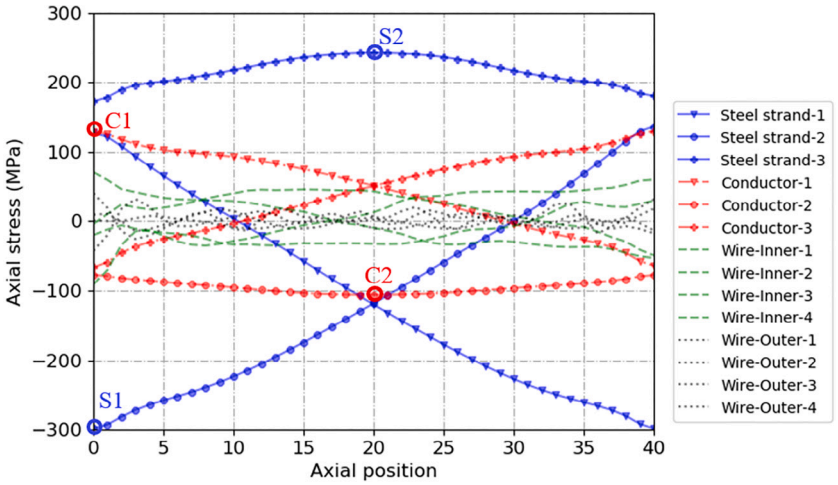

Fig. 28. Axial stress of the metals when t = 1 s.

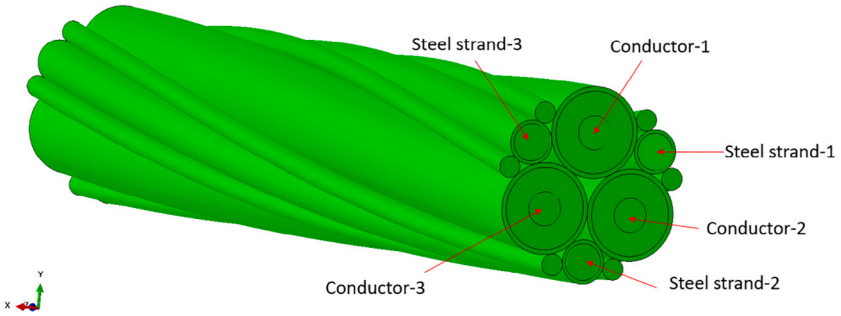

Fig. 29. Illustration of all the inner metals.

CRediT authorship contribution statement

Pan Fang: Writing – review & editing, Writing – original draft, Visualization, Validation, Software, Methodology, Investigation, Formal analysis, Data curation, Conceptualization. **Xiao Li:** Writing – review & editing, Investigation. **Xiaoli Jiang:** Writing – review & editing, Supervision, Project administration, Funding acquisition. **Hans Hopman:** Writing – review & editing, Supervision, Project administration. **Yong Bai:** Writing – review & editing, Supervision, Project administration, Funding acquisition.

Declaration of competing interest

The authors declare the following financial interests/personal relationships which may be considered as potential competing interests: Pan Fang reports financial support was provided by China Scholarship Council [grant number 201906320047]

Acknowledgement

The first author would like to express gratitude for the support from the China Scholarship Council [grant number 201906320047] and Orient Cable (NBO) in providing the test samples.

Data availability

Data will be made available on request.

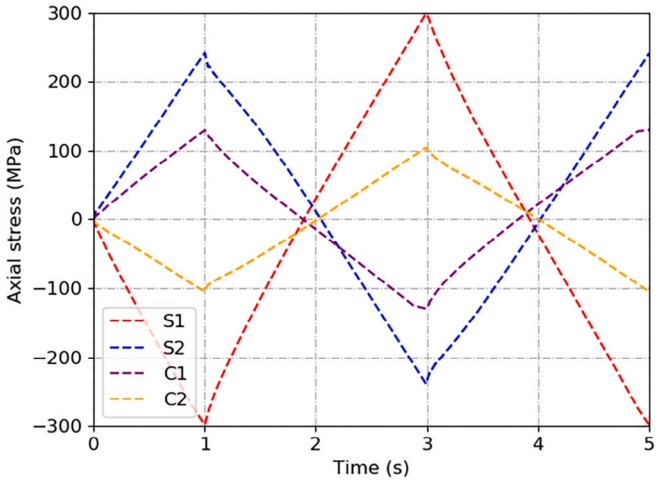

Fig. 30. The stress variation of the four feature points.

References

[1] Carbon Trust. Floating wind joint industry project – phase 2 summary report. 2020, https://www.carbontrust.com/our-work-and-impact/guides-reports-and-tools/floating-wind-joint-industry-project-phase-2-summary-report. [Accessed 02 April 2025].

[2] Young D, Ng C, Oterkus S, Li Q, Johanning L. Assessing the mechanical stresses of dynamic cables for floating offshore wind applications. In: Journal of physics: conference series. 1102, (1):IOP Publishing; 2018, 012016.

[3] Rentschler MU, Adam F, Chainho P. Design optimization of dynamic inter-array cable systems for floating offshore wind turbines. Renew Sustain Energy Rev 2019;111:622–35.

[4] WindEurope. The EU offshore renewable energy strategy. 2025, https://windeurope.org/policy/position-papers/the-eu-offshore-renewable-energy-strategy/. [Accessed 02 April 2025].

[5] ETIPWind. Roadmap. 2019, https://etipwind.eu/roadmap/. [Accessed 02 April 2025].

[6] Ech-Cheikh F, Drissi-Habti M. Numerical modeling of the micromechanics damage of an offshore electrical high-voltage phase. Energies 2023;16(14):5422.

[7] Nasution FP, Sævik S, Gjøsteen JK. Study of fatigue strength of copper conductor considering irregularities surfaces by experimental testings and fe-analysis. In: International conference on offshore mechanics and arctic engineering. 44908, American Society of Mechanical Engineers; 2012, p. 269–75.

[8] Nasution FP, Sævik S, Gjøsteen JK. Fatigue analysis of copper conductor for offshore wind turbines by experimental and FE method. Energy Procedia 2012;24:271–80.

[9] Jiang K, Bai Y, Cheng P. Fatigue life estimation of stranded copper conductors using the method based on the fatigue damage evolution model. Ships Offshore Struct 2023;1–13.

[10] Miceli M, Carvelli V, Drissi-Habti M. Modelling electro-mechanical behaviour of an XLPE insulation layer for hi-voltage composite power cables: Effect of voids on onset of coalescence. Energies 2023;16(12):4620.

[11] Ech-Cheikh F, Matine A, Drissi-Habti M. Preliminary multiphysics modeling of electric high-voltage cable of offshore wind-farms. Energies 2023;16(17):6286.

[12] Young DG. Predicting failure of dynamic offshore cables by insulation breakdown due to water treeing. 2020.

[13] Fang P, Li X, Jiang X, Hopman H, Bai Y. Bending study of submarine power cables based on a repeated unit cell model. Eng Struct 2023;293:116606.

[14] Fang P, Li X, Jiang X, Hopman H, Bai Y. Development of an effective modeling method for the mechanical analysis of three-core submarine power cables under tension. Eng Struct 2024;317:118632.

[15] Ménard F, Cartraud P. A computationally efficient finite element model for the analysis of the non-linear bending behaviour of a dynamic submarine power cable. Mar Struct 2023;91:103465.

[16] Tjahjanto DD, Tyrberg A, Mullins J. Bending mechanics of cable cores and fillers in a dynamic submarine cable. In: International conference on offshore mechanics and arctic engineering. 57694, American Society of Mechanical Engineers; 2017, V05AT04A038.

[17] Leroy J-M, Poirette Y, Brusselle Dupend N, Caleyron F. Assessing mechanical stresses in dynamic power cables for floating offshore wind farms. In: International conference on offshore mechanics and arctic engineering. 57786, American Society of Mechanical Engineers; 2017, V010T09A050.

[18] Fang P, Jiang X, Hopman H, Bai Y. Mechanical responses of submarine power cables subject to axisymmetric loadings. Ocean Eng 2021;239:109847.

[19] Sævik S. A finite element model for predicting stresses and slip in flexible pipe armouring tendons. Comput Struct 1993;46(2):219–30.

[20] Love AEH. A treatise on the mathematical theory of elasticity. University Press; 1927.

[21] Kirchhoff G. Über das Gleichgewicht und die Bewegung eines unendlich dünnen Stabes. J F Math 1858;291.

[22] Skeie G, Sødahl N, Steinkjer O, et al. Efficient fatigue analysis of helix elements in umbilicals and flexible risers: Theory and applications. J Appl Math 2012;2012.

[23] DNV-GL. SESAM white paper–Helica, cross section analysis of compliant structures–flexibles, umbilicals and cables. 2016, Hövik, Norway.

[24] Bussolati F. Modèle multi-échelle de la fatigue des lignes d'ancrage câblées pour l'éolien offshore flottant (Ph.D. thesis), Université Paris-Saclay (ComUE); 2019.

[25] Ménard F, Cartraud P. Solid and 3D beam finite element models for the non-linear elastic analysis of helical strands within a computational homogenization framework. Comput Struct 2021;257:106675.

[26] CIGRE. Offshore generation cable connections. 2025, https://www.researchgate.net/publication/3383888640_CIGRE_TB_610_-_Offshore_generation_cable_connections/citations. [Accessed 02 April 2025].

[27] Taihan Cable & Solution Co, Ltd. Power generation. 2022, https://www.taihan.com/en/business/product/productDetail?idx=20. [Accessed 02 April 2025].

[28] NEXANS. Subsea cables — MV medium voltage power & fibre optics cables. 2019, https://www.powerandcables.com/subsea-cables-joints-terminations/. [Accessed 02 April 2025].

[29] Chang H-C, Chen B-F. Mechanical behavior of submarine cable under coupled tension, torsion and compressive loads. Ocean Eng 2019;189:106272.

[30] API. API 17B: recommended practice for flexible pipe. American Petroleum Institute; 2014.

[31] Tyrberg A, Tjahjanto D, Hedlund J. Bend stiffness of submarine cables—An experimental and numerical investigation. In: Proceedings of the 10th international conference on insulated power cables. 2019.

[32] Bai Y, Liu T, Ruan W, Chen W. Mechanical behavior of metallic strip flexible pipe subjected to tension. Compos Struct 2017;170:1–10.

[33] Bahtui A, Bahai H, Alfano G. Numerical and analytical modeling of unbonded flexible risers. 2009.

[34] Abaqus G. Abaqus 6.11. Dassault Systemes Simulia Corporation, Providence, RI, USA 2011;3:73.

[35] Dai T, Sævik S, Ye N. Friction models for evaluating dynamic stresses in non-bonded flexible risers. Mar Struct 2017;55:137–61.

[36] Wróbel G, Szymiczek M. Influence of temperature on friction coefficient of low density polyethylene. J Achiev Mater Manuf Eng 2008;28(1):31–4.

[37] Feyzullahoglu E, Saffak Z. The tribological behaviour of different engineering plastics under dry friction conditions. Mater Des 2008;29(1):205–11.

[38] Fang P, Yuan S, Cheng P, Bai Y, Xu Y. Mechanical responses of metallic strip flexible pipes subjected to pure torsion. Appl Ocean Res 2019;86:13–27.

[39] Zhang X, Wang S, Ma W, Su L, Yang Y. Study on the influence of bending curvature on the bending characteristics of unbonded flexible pipes. Ocean Eng 2023;281:114730.

[40] Knapp R. Tension and bending fatigue modeling of cables. In: ISOPE international ocean and polar engineering conference. ISOPE; 2004, p. ISOPE–I.

[41] Jeroense M. Recommendations for mechanical testing of submarine cables (and their accessories). 2023, http://dx.doi.org/10.1007/978-3-030-80406-0_5.

[42] Zhang M, Chen X, Fu S, Guo Y, Ma L. Theoretical and numerical analysis of bending behavior of unbonded flexible risers. Mar Struct 2015;44:311–25.

[43] Kraincanic I, Kebadze E. Slip initiation and progression in helical armouring layers of unbonded flexible pipes and its effect on pipe bending behaviour. J Strain Anal Eng Des 2001;36(3):265–75.

[44] Ma W, Su L, Wang S, Yang Y, Huang W. Influence of structural parameters of unbonded flexible pipes on bending performance. Ocean Eng 2022;266:113109.

[45] Fernando US, Tan Z, Sheldrake T, Clements R. The stress analysis and residual stress evaluation of pressure armour layers in flexible pipes using 3D finite element models. In: International conference on offshore mechanics and arctic engineering, vol. 37459, 2004, p. 57–65.

[46] Wang L, Yue Q. A full layered numerical model for predicting hysteretic behavior of unbonded flexible pipes considering initial contact pressure. Appl Ocean Res 2021;111:102626.

[47] Lu H, Vaz MA, Caire M. A finite element model for unbonded flexible pipe under combined axisymmetric and bending loads. Mar Struct 2020;74:102826.

[48] Wang L, Ye N, Yue Q. A novel helix contact model for predicting hysteretic behavior of unbonded flexible pipes. Ocean Eng 2022;264:112407.

[49] Cartraud P, Messager T. Computational homogenization of periodic beam-like structures. Int J Solids Struct 2006;43(3–4):686–96.

[50] Kolpakov A. Calculation of the characteristics of thin elastic rods with a periodic structure. J Appl Math Mech 1991;55(3):358–65.

[51] Buannic N, Cartraud P. Higher-order effective modeling of periodic heterogeneous beams. I. Asymptotic expansion method. Int J Solids Struct 2001;38(40–41):7139–61.

[52] Buannic N, Cartraud P. Higher-order effective modeling of periodic heterogeneous beams. II. Derivation of the proper boundary conditions for the interior asymptotic solution. Int J Solids Struct 2001;38(40–41):7163–80.

[53] Rahmati M, Bahai H, Alfano G. An accurate and computationally efficient small-scale nonlinear FEA of flexible risers. Ocean Eng 2016;121:382–91.
[54] Diehl T. Formulation of a user MPC to simulate beam-type transport problems. Tech. rep., MFSP Internal Report, Department of Mechanical Engineering, University of Rochester; 1993.
[55] Krenk S. Non-linear modeling and analysis of solids and structures. Cambridge University Press; 2009.
[56] Strogatz SH. Nonlinear dynamics and chaos with student solutions manual: With applications to physics, biology, chemistry, and engineering. CRC Press; 2018.
[57] DELFTBLUE. Delft high performance computing centre (DHPC), DelftBlue supercomputer(phase 1). 2022, URL https://www.tudelft.nl/dhpc/ark/delftbluephase1.
[58] Paumier L, Averbuch D, Felix-Henry A. Flexible pipe curved collapse resistance calculation. In: International conference on offshore mechanics and arctic engineering, vol. 43437, 2009, p. 55–61.
[59] Wang H, Hebert CB, Barbato G, Silveira L, dos Santos Paiva MV, Coser TB, López FS, Strohaecker TR, Bertoni F. Submarine power cable design validation through model testing. In: ISOPE international ocean and polar engineering conference. ISOPE; 2016, p. ISOPE–I.